



THE ROLE OF SiO AS A TRACER OF PAST STAR FORMATION EVENTS: THE CASE OF THE HIGH-MASS PROTOCLUSTER NGC 2264-C

ANA LÓPEZ-SEPULCRE¹, YOSHIMASA WATANABE¹, NAMI SAKAI², RYUTA FURUYA¹,
OSAMU SARUWATARI¹, AND SATOSHI YAMAMOTO¹

¹ Department of Physics, The University of Tokyo, 7-3-1 Hongo, Bunkyo-ku, Tokyo, 113-0033, Japan; ana@taurus.phys.s.u-tokyo.ac.jp

² RIKEN, S407 Chemistry and Materials Physics Building, 2-1 Hirosawa, Wako, Saitama, 351-0198, Japan

Received 2015 December 25; accepted 2016 March 15; published 2016 May 10

ABSTRACT

NGC 2264-C is a high-mass protocluster where several star formation events are known to have occurred. To investigate whether past protostellar activity has left a chemical imprint in this region, we mapped it in SiO ($J = 2 - 1$), which is a shock tracer, and several other molecular lines with the Nobeyama 45 m telescope. Our observations show the presence of a complex network of protostellar outflows. The strongest SiO emission lies beyond a radius of ~ 0.1 pc with respect to the center of the clump and is characterized by broad (> 10 km s⁻¹) lines and abundances of $\sim 1.4 \times 10^{-8}$ with respect to H₂. Interestingly, SiO appears to be relatively depleted ($\chi_{\text{SiO}} \sim 4 \times 10^{-9}$) within this radius, despite it being affected by molecular outflow activity. We attribute this to the fast condensation of SiO back onto dust grains and/or rapid gas-phase destruction of SiO, which is favored by the high density present in this area ($> 10^6$ cm⁻³). Finally, we identify a peripheral, narrow-line (~ 2 km s⁻¹) component where SiO has an abundance of a few times 10^{-11} . After considering different options, we conclude that this weak emission may be tracing protostellar shocks from the star formation episode that preceded the current one, which have decelerated over time and eventually resulted in SiO being largely depleted/destroyed. Alternatively, a population of unresolved, low-mass protostars may be responsible for the narrow SiO emission. High-angular resolution observations are necessary to distinguish between these two possibilities, and thus to understand the role of SiO as a chemical tracer of past star formation episodes in massive protoclusters.

Key words: ISM: abundances – ISM: individual objects (NGC 2264) – ISM: jets and outflows – ISM: molecules – stars: formation

1. INTRODUCTION

1.1. High-mass Star and Cluster Formation

There is substantial evidence that most stars in our Galaxy form in clustered environments rather than in isolation (e.g., Lada & Lada 2003). These populated environments, or protoclusters, are excellent laboratories in which to study a variety of physical and chemical processes, such as cloud fragmentation and feedback from young (proto-)stars onto their surroundings (see Krumholz et al. 2014 for a review). Moreover, high-mass stars ($M_* > 8 M_\odot$) tend to form in dense clusters. The study of protoclusters is therefore essential if we aim to investigate the dominant star formation mode in our Galaxy and, in particular, the formation of high-mass stars, which still poses some major questions.

One such major question is how a massive molecular core can evolve without fragmenting into smaller cores. Some solutions have been proposed, such as radiative feedback or heating from a first generation of low-mass (proto-)stars (Krumholz et al. 2007; Krumholz & McKee 2008; Longmore et al. 2011). If this is the case, then an episode of low-mass star formation should precede the formation of massive stars. This implies that the molecular cloud hosting such a protocluster should resist global gravitational collapse long enough to allow for the formation of more than one generation of protostars. In short, some forces must be present that counterbalance gravity on protocluster scales (~ 1 pc) for several free-fall times.

Turbulent motions within molecular clouds may provide an effective source of energy acting against gravity. In particular, protostellar feedback has been proposed to be a potentially dominant source of turbulence replenishment in active

protoclusters. Li & Nakamura (2006) performed three-dimensional (3D) magneto-hydrodynamic simulations of cluster formation, and found that the initial cloud turbulence is quickly replaced by motions generated by outflows, thus keeping the cloud stable against gravitational collapse long after the initial turbulence has dissipated. Other theoretical and observational studies that followed lend further support to this finding (e.g., Matzner 2007; Nakamura & Li 2007; Stanke & Williams 2007; Nakamura et al. 2011). In the present study, we target an active, high-mass protocluster where such a scenario may be taking place: NGC 2264-C.

1.2. The Target: NGC 2264-C

NGC 2264-C is a molecular clump located at a distance of 740 pc (Kamezaki et al. 2014) which is known to be surrounded by a large cluster of pre-main-sequence stars (e.g., Sung et al. 1997; Rebull et al. 2002; Sung et al. 2008). It contains multiple dense cores amounting to a total mass of $1650 M_\odot$ (Peretto et al. 2006), and very complex CO line-wing components from multiple molecular outflows (Maury et al. 2009). At the geometrical center of the clump lies the most massive molecular core in this site, CMM3 ($50 M_\odot$), which is thought to be the precursor of a high-mass star. Saruwatari et al. (2011) proposed that it is a very young massive protostellar candidate based on the discovery of a compact CO outflow with a dynamical age of a few hundred years. More recently, Watanabe et al. (2015) reported further evidence of the core's youth based on its chemical composition, which displays high abundances of deuterated molecules and carbon chains relative to those measured in Orion KL, and low abundances of complex organic molecules.

In summary, there is considerable evidence suggesting that NGC 2264-C has experienced more than one episode of star formation, with one of the latest episodes potentially being that of a massive star. This region therefore appears to be a clear case where low-mass star formation precedes high-mass star formation, and where protostellar outflows may have provided the necessary amount of turbulence to avoid fast cloud collapse.

1.3. SiO, A Tracer of Protostellar Activity

Protostellar outflow activity may leave a molecular trace on its host cloud that might take a long time to erase completely. Our goal here is to assess whether SiO can be used as such a tracer in NGC 2264-C. If so, then it could provide an astrochemical means to evaluate the presence of old protostellar activity and past star formation episodes in other high-mass star formation sites hosting very young, massive cores.

The choice of SiO for this study relies on its association with shocks, in particular, with those originating from protostellar outflows (e.g., Gueth et al. 1998; Codella et al. 2007; Tafalla et al. 2015). Indeed, the abundance of SiO in the gas phase can be enhanced by several orders of magnitude in protostellar shocks due to sputtering of Si atoms from grains or direct vaporization of SiO from grain mantles (e.g., Gusdorf et al. 2008; Guillet et al. 2009; Anderl et al. 2013). Since the SiO depletion time back onto the grains, as well as the timescale for its gas-phase destruction, is quite fast in protostellar regions (typically $\sim 10^4$ years; Bergin et al. 1998; Pineau des Forêts et al. 1997), this molecule should be preferentially enhanced close to shocks and should therefore be associated with high velocities. However, a typically extended, narrow-line component has also been detected in a number of star-forming regions. This may be associated with past high-velocity shocks that have decelerated with time and have not yet suffered complete depletion (e.g., Codella et al. 1999), although other explanations are possible, such as low-velocity shocks caused by large-scale flow collisions during global collapse or by the dynamical interaction of two clouds (Jiménez-Serra et al. 2010, Sanhueza et al. 2013).

With all the above in mind, we have mapped NGC 2264-C in SiO($J = 2 - 1$) and other molecular tracers with the Nobeyama 45 m telescope. The observations are described in Section 2. Maps and spectra are presented in Section 3, and a quantitative analysis is provided in Section 4. We discuss our results in Section 5 and conclude in Section 6.

2. OBSERVATIONS

We obtained maps of NGC 2264-C in SiO($J = 2 - 1$), CH₃OH($2_0 - 1_0$ A⁺), and H¹³CO⁺($J = 1 - 0$) with the Nobeyama 45 m telescope at the Nobeyama Radio Observatory (NRO) in 2009 March (SiO) and 2011 April–May (CH₃OH and H¹³CO⁺). The side-band-separating (2SB) mixer receiver T100H/V was used as a frontend with typical system noise temperatures of 160–360 K and 160–270 K for the SiO and CH₃OH/H¹³CO⁺ observations, respectively. The beam size of the Nobeyama 45 m telescope was 19'' at 86 GHz. The main-beam efficiency (η_{mb}) was 42%. The backends used were the acousto-optical radio spectrometers AOS-H, whose bandwidth and frequency resolution were 40 MHz and 37 kHz, respectively. The position switch method was employed with an off position of (R.A. offset, decl. offset) = (+2', +30'). The

intensity scale was calibrated to the antenna temperature (T_{A}^*) scale using the chopper-wheel method and its accuracy is estimated to be 20%. The telescope pointing was checked every hour by observing the SiO maser source GX Mon. The pointing accuracy is confirmed to be better than 5''. The mapped area is about $4'.2 \times 4'.2$ centered at (R.A., decl.) = (06^h41^m12^s.3, +09°29'12'') with a grid spacing of 19''. At the central $1'.4 \times 1'.6$ of the SiO map, the grid spacing is a nyquist grid of 9''.5.

The data were reduced using the software package NEWS-TAR, developed by NRO. After subtracting the baseline via first-order polynomial fitting, final spectra were obtained for each position in the map. The T_{A}^* scale was converted to the main-beam brightness temperature (T_{mb}) scale by $T_{\text{mb}} = T_{\text{A}}^*/\eta_{\text{mb}}$.

We observed CO($J = 1 - 0$) in 2012 March with the Nobeyama 45 m telescope. The T100H/V receiver was used as the frontend with a typical system noise temperature of 250–280 K. The resulting beam size of the NRO 45 m telescope was 15'' at 115 GHz. The main-beam efficiency (η_{mb}) was 33%. The backends used were the SAM45 autocorrelators, whose bandwidth and frequency resolution were 125 MHz and 30.52 kHz, respectively. The on-the-fly mapping method (Sawada et al. 2008) was employed to cover a $3' \times 4'$ area centered at (R.A., decl.) = (06^h41^m12^s.3, +09°29'12''), with the off position being (R.A. offset, decl. offset) = (+2', +30'). In order to reduce the noise derived from scanning effects, we obtained two CO maps with two different orthogonal scanning directions and combined them in the data reduction procedure. The intensity scale was calibrated to the T_{A}^* scale using the chopper-wheel method. The T_{A}^* scale was converted to the T_{mb} scale using $T_{\text{mb}} = T_{\text{A}}^*/\eta_{\text{mb}}$. The pointing accuracy is better than 5'' based on observations of the SiO maser source GX Mon.

The data were reduced using the software package NOSTAR (Sawada et al. 2008), developed by NRO. After subtracting the baseline via first-order polynomial fitting, the data were re-sampled with a grid size of 6'' and integrated. In the re-sampling procedure, the angular resolution was broadened to $\sim 19''.5$.

The observed molecular transitions are listed in Table 1, along with their properties. The average systemic velocity of NGC 2264-C is 7.5 km s⁻¹.

3. RESULTS

3.1. Integrated Maps and Spectra

Figure 1 presents the integrated SiO($J = 2 - 1$) map of NGC 2264-C (color scale), which was obtained by integrating the emission of each velocity channel with a signal-to-noise ratio (S/N) above or equal to 5 in the channel map. Overlaid on the map are the corresponding spectra at each observed offset position. Analogous maps are shown in the lower panels of Figure 1 for H¹³CO⁺($J = 1 - 0$) and CH₃OH($2_0 - 1_0$ A⁺) (hereafter H¹³CO⁺ and CH₃OH, respectively).

Columns 2 and 3 in Table 2 list the velocity ranges used to obtain the integrated maps and the resulting rms noise. Note the wide velocity range of SiO emission relative to that of H¹³CO⁺, which indicates a clear association of the former with high-velocity gas. In the case of CH₃OH, due to blending with two other methanol lines, we employed the same velocity range

Table 1
Molecular Lines Observed^a

Molecule	Transition	ν_0 (MHz)	E_u (K)	A_{ul} (s ⁻¹)	δV^b (km s ⁻¹)	θ_{beam} ($''$)	rms Noise ^c (mK)
H ¹³ CO ⁺	$J = 1 - 0$	86754.288	4.2	3.9×10^{-5}	0.5	19.5	91
SiO	$J = 2 - 1$	86846.985	6.3	2.9×10^{-5}	0.5	19.5	54
CH ₃ OH	$2_{-1} - 1_{-1} E$	96739.362	12.5	2.6×10^{-6}	0.5	17.5	50
CH ₃ OH	$2_0 - 1_0 A^+$	96741.375	7.0	3.4×10^{-6}	0.5	17.5	50
CH ₃ OH	$2_{+0} - 1_{+0} E$	96744.550	20.1	3.1×10^{-6}	0.5	17.5	50
CO	$J = 1 - 0$	115271.20	5.5	7.2×10^{-8}	0.5	14.7	530

Notes.

^a The three CH₃OH lines are blended with each other. Throughout this paper, we use only the central velocities of the $(2_0 - 1_0)A^+$ transition.

^b Channel width after spectral smoothing for a higher signal-to-noise ratio.

^c Main beam temperature (T_{mb}) units.

as for H¹³CO⁺. This includes only the central velocity channels and excludes the emission from the line wings.

A first glance at the SiO, H¹³CO⁺, and CH₃OH maps immediately reveals how differently these three molecules trace the region. While H¹³CO⁺ mostly traces the central area of NGC 2264-C where the gas is denser (see Peretto et al. 2006), SiO primarily emits in a more peripheral area and appears to be depleted at the center. CH₃OH, on the other hand, is enhanced both at the center and on the periphery. This suggests that, in this source, CH₃OH traces both dense gas (as H¹³CO⁺) and shocked regions (as SiO).

3.2. Three SiO Components

In order to understand the spatial distribution and nature of the SiO emission in NGC 2264-C, we examined both its line intensity and width, relative to those of H¹³CO⁺. To this aim, Figure 2 presents two images: the SiO-to-H¹³CO⁺ integrated map (left), and the SiO-to-H¹³CO⁺ moment 2—or line width—map (right). The former was obtained using the same velocity interval for both SiO and H¹³CO⁺ (ΔV_{ctr} in Table 2), while for the latter we used the entire velocity ranges with emission above 5σ (ΔV_{tot} in Table 2). The plotted area comprises all of the positions where the emission of SiO exceeds an S/N of 3. Within this area, the S/N of the H¹³CO⁺ emission always exceeds 15.

Figures 1 and 2 (left) clearly show how the strongest SiO emission is offset with respect to the massive molecular core CMM3 at the center of NGC 2264-C, thus tracing a relatively peripheral area of the molecular clump. From Figure 2 (right), one may note that the width of the SiO line also tends to be broad in this area, more than twice that of H¹³CO⁺. This region is thus characterized by high-velocity shocks that are likely the result of a complex network of protostellar outflows within NGC 2264-C. Close to CMM3, the SiO line emission is weaker but nevertheless broad, also suggesting the presence of high-velocity shocks. Finally, further out with respect to the enhanced SiO emission region, there is an area where SiO lines are both relatively weak and narrow, especially toward the north and north-west. Indeed, the line width of SiO in this external area is comparable to that of H¹³CO⁺. Thus, overall, we can distinguish between three different SiO components.

1. Broad-line SiO component (hereafter broad or B): it comprises the area where the emission of SiO is most prominent. The SiO lines have full-widths at zero power

(FWZP) between 20 and 40 km s⁻¹. This component is spatially offset with respect to the center of the molecular clump, which, together with the high-velocity SiO line wings associated with it, indicates the presence of a circumcluster shocked region due to protostellar activity within the molecular clump.

2. Central SiO component (hereafter central or C): it lies at the center of the clump, around the molecular cores CMM3 and CMM13, where the gas is densest according to Peretto et al. (2006). It is characterized by weaker SiO emission than the broad component, but it also displays high-velocity line wings suggestive of protostellar outflows, with FWZP typically between 20 and 25 km s⁻¹.
3. Narrow-line SiO component (hereafter narrow or N): it is located at the very periphery of NGC 2264-C, and it exhibits weak and narrow (~ 2 km s⁻¹) SiO lines relative to H¹³CO⁺.

For reference, Figure 3 shows sample spectra for each of the three different components, extracted at the positions indicated in the figure caption and labeled in Figure 2 (B4, C1, and N2). Following the above classification, in Figure 2, we have selected and marked several positions that are representative of each of the three SiO components, whose molecular spectra are used in Section 4 to derive their respective molecular column densities and abundances. Some of these coincide with molecular cores identified by Peretto et al. (2006, 2007). For example, CMM3 and CMM13 are two of the selected positions representing the central component. Table 3 lists the offset coordinates, velocity ranges with emission above S/N = 3, and line fluxes measured at each of these positions. The numbers in parentheses are the measured flux errors, which account for the rms noise of the observations and the calibration uncertainty.

3.3. Outflow Maps

High-velocity SiO emission is widely present across ~ 0.5 pc in NGC 2264-C. This strongly supports a large amount of protostellar outflow activity, as reported by Maury et al. (2009) based on CO($J = 2 - 1$) observations. We have obtained SiO ($J = 2 - 1$) and CO($J = 1 - 0$) outflow maps by integrating the blue- and redshifted high-velocity emission of the lines. These are presented in Figure 4.

Since CH₃OH is blended with other methanol lines, an outflow assessment from this molecular tracer is unreliable. Nevertheless, a qualitative analysis of the unblended blue- and

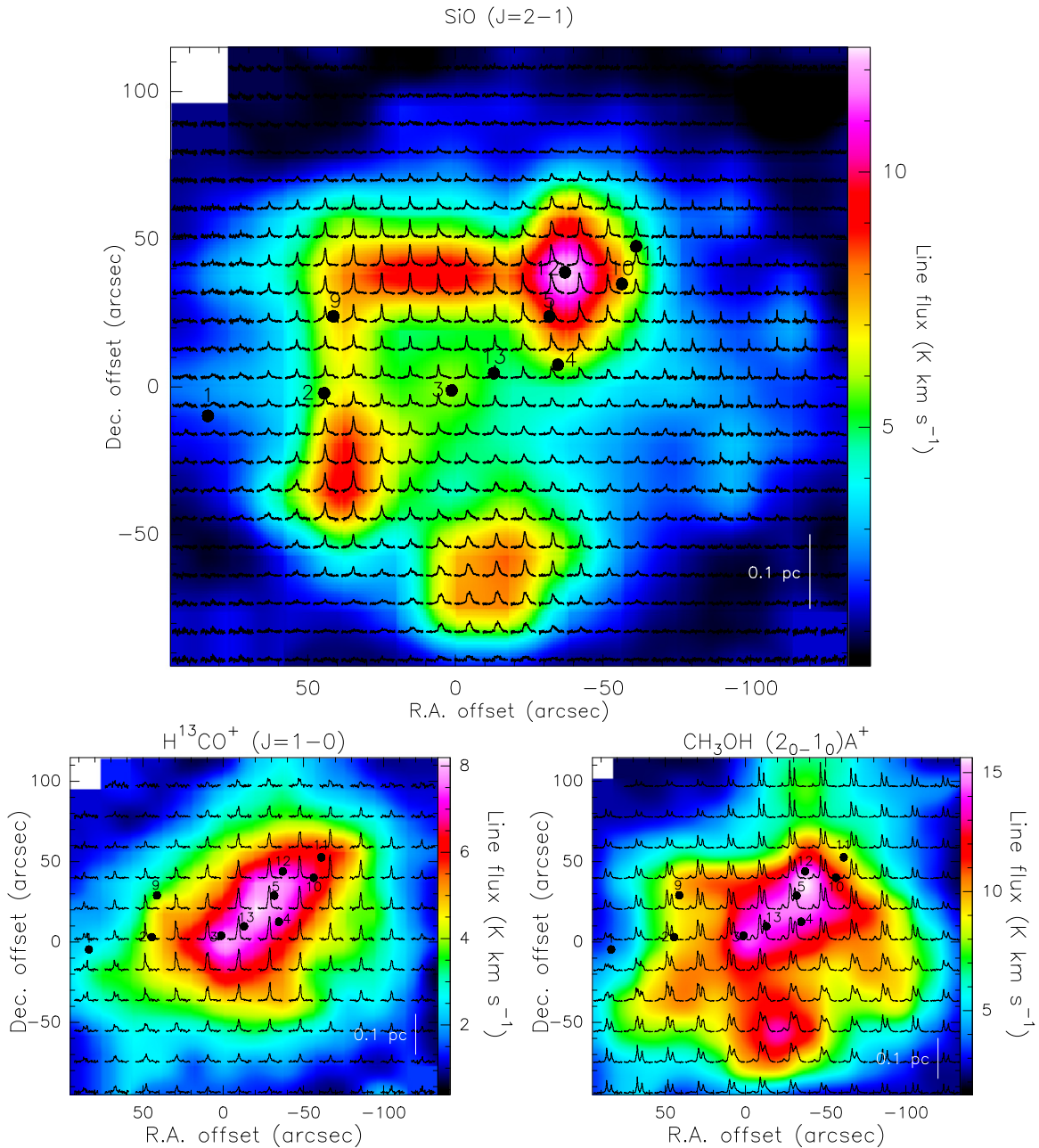


Figure 1. Spectral line maps of $\text{SiO}(J=2-1)$, $\text{H}^{13}\text{CO}^+(J=1-0)$, and $\text{CH}_3\text{OH}(2_0-1_0)A^+$ at intervals of $9''5$, $19''$, and $19''$, respectively, overlaid on the corresponding velocity-integrated maps (color scale). The velocity ranges used to obtain the maps are $[-1.3, 20.3] \text{ km s}^{-1}$ for SiO and $[+5.5, +10.5] \text{ km s}^{-1}$ for H^{13}CO^+ and CH_3OH (see Table 2). Black circles mark the positions of the millimeter cores identified by Peretto et al. (2006, 2007). The reference ($0''$, $0''$) position corresponds to CMM3: R.A.(J2000) = $06^{\text{h}}41^{\text{m}}12^{\text{s}}.3$, decl.(J2000) = $09^{\circ}29'11''.90$.

redshifted line wings from the two E-state transitions of CH_3OH (see the spectra in Figure 3) shows that they are not as prominent as those of SiO , which span more than 10 km s^{-1} from the ambient velocities. The outflow maps using the unblended line wings of methanol show a distribution similar to that of SiO (Figure 4). However, since this emission arises from two lines that are not considered in the analysis below, we do not present the maps here. For $\text{CO}(J=1-0)$, the line wings are not as extended either, but this is most likely due to the much lower sensitivity—by a factor 10—of the observations for this molecule (see Table 1).

The outflow maps in Figure 4 show how the spatial distribution of the blue- and redshifted high-velocity emission

is rather complex. The blueshifted emission is dominant toward the east of the clump, while the redshifted emission concentrates mostly toward the west. Unfortunately, the angular resolution of our observations does not allow us to clearly separate the individual molecular outflows and associate them with particular molecular cores. Instead, the maps show a tangled circumcluster shock network. Despite this, hints of the very collimated molecular outflow, defined by Maury et al. (2009) as flows F1 (redshifted; north of CMM13) and F2 (blueshifted; south of CMM13), are evident in our CO outflow map. It should be noted that the CO emission may be moderately optically thick even at the high-velocity wings (see Section 4.2).

Table 2
Velocity Ranges and rms Noise of the Integrated Maps

Tracer	All Channels Above 5σ		Central Velocities		Outflow Blue- and Redshifted Wings			
	ΔV_{tot} (km s $^{-1}$)	σ_{tot} (K km s $^{-1}$)	ΔV_{ctr}^a (km s $^{-1}$)	σ_{ctr} (K km s $^{-1}$)	ΔV_{b} (km s $^{-1}$)	σ_{b} (K km s $^{-1}$)	ΔV_{r} (km s $^{-1}$)	σ_{r} (K km s $^{-1}$)
H 13 CO $^+$	[5.5, 10.5]	0.046	[5.5, 10.5]	0.046
SiO	[-1.3, 20.3]	0.12	[5.5, 10.5]	0.087	[-1.3, 5.5]	0.099	[10.5, 20.3]	0.12
CH $_3$ OH b	[5.5, 10.5]	0.062
CO c	[-1.0, 21.0]	1.1	[-1.0, 5.5]	0.84	[10.5, 21.0]	1.0

Notes.

^a The velocity range is determined by the channels with emission above 5σ in the H 13 CO $^+$ line.

^b The line wings are blended with other methanol lines (see Table 1).

^c The central velocities are not indicated nor used throughout the paper due to heavy self-absorption.

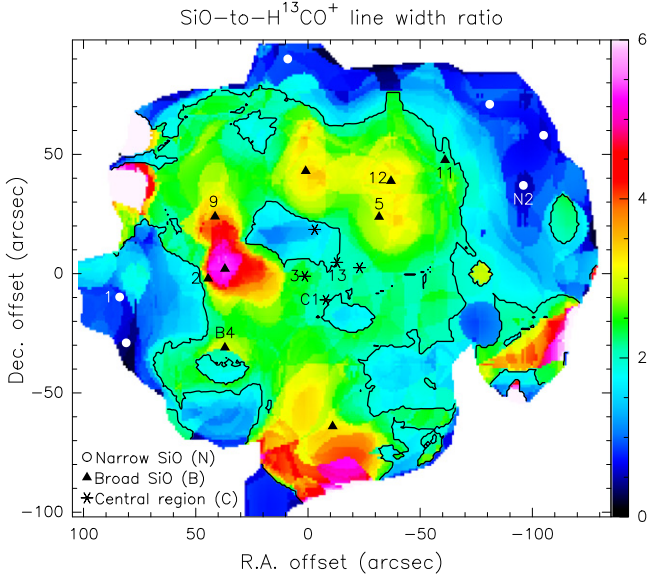


Figure 2. SiO-to-H 13 CO $^+$ moment 2 map within the area where the SiO emission exceeds $S/N = 3$. The black contour marks our adopted dividing line between the narrow and broad SiO line profiles, corresponding to an SiO-to-H 13 CO $^+$ line width ratio of 2. The positions where we have extracted spectra for the analysis are marked with white circles (narrow component), black triangles (broad component), and asterisks (central component; see Section 3.2 for details). The numbers indicate the labels of the millimeter cores as reported by Peretto et al. (2006, 2007).

4. DERIVATION OF COLUMN DENSITIES AND ABUNDANCES

In order to evaluate the nature of the different SiO components identified in Section 3.2, here we provide an estimate of molecular column densities and abundances at each selected position (Table 3).

4.1. Column Density of the Narrow Component

Under the assumption of Local Thermodynamic Equilibrium, the total column density of a given molecule, N , is described by Boltzmann's equation as

$$N = \frac{N_u}{g_u} Q(T_{\text{ex}}) e^{-\frac{E_u}{kT_{\text{ex}}}}, \quad (1)$$

where N_u , g_u , T_{ex} , $Q(T_{\text{ex}})$, E_u , and k are, respectively, the column density of the upper energy state, its degeneracy, the excitation temperature describing the level populations, the

partition function at a given T_{ex} , the energy of the upper state, and Boltzmann's constant.

The column density of the upper energy state is given by

$$N_u = \frac{8\pi\nu^3}{c^3} \frac{1}{A_{ul}} \frac{1}{e^{\frac{h\nu}{kT_{\text{ex}}}} - 1} \int \tau dv, \quad (2)$$

where ν , c , A_{ul} , h , and $\int \tau dv$ are the frequency of the transition, speed of light, Einstein coefficient for spontaneous emission, Planck's constant, and the velocity-integrated optical depth of the molecular line, respectively. With only one observed transition per molecule, we have no means of constraining T_{ex} . We therefore adopt three different values: $T_{\text{ex}} = 10, 20,$ and 40 K. For each of these values, and for each molecular tracer, we have estimated the integrated optical depth as the discrete summation of the optical depth at each velocity channel, n , of constant width $\delta\nu$:

$$\sum_n \tau_n \delta\nu = -\delta\nu \sum_n \ln \left(1 - \frac{T_{\text{mb}}}{J_\nu(T_{\text{ex}}) - J_\nu(T_{\text{bg}})} \right). \quad (3)$$

Here, T_{mb} is the main-beam temperature of the line for a given channel n , and $J_\nu(T)$ is defined as

$$J_\nu(T) = \frac{h\nu}{k} \frac{1}{e^{\frac{h\nu}{kT}} - 1}. \quad (4)$$

Table 3 lists the velocity ranges used to integrate the emission and obtain the column density of SiO, CH $_3$ OH, and H 13 CO $^+$ in the six positions selected to represent the narrow component. These ranges comprise the velocity channels where the emission of H 13 CO $^+$, which displays no high-velocity wings, exceeds 3σ . In the case of CMM1, the emission is double peaked, and hence a wide velocity range is measured.

The resulting column densities for each of the three adopted values of T_{ex} are presented in Table 4. Since the central velocities of CO($J = 1 - 0$) correspond to heavily self-absorbed emission in most of the mapped area, we do not consider them here. Instead, we will analyze the emission of the CO high-velocity line wings in Section 4.2.

4.2. Column Density of the Broad and Central Components

Following a procedure analogous to that described in Section 4.1, we derived the SiO and CO column densities at each selected position of the broad and central components, which trace high-velocity molecular gas from the protocluster activity. For CO, we integrated the line emission only at the

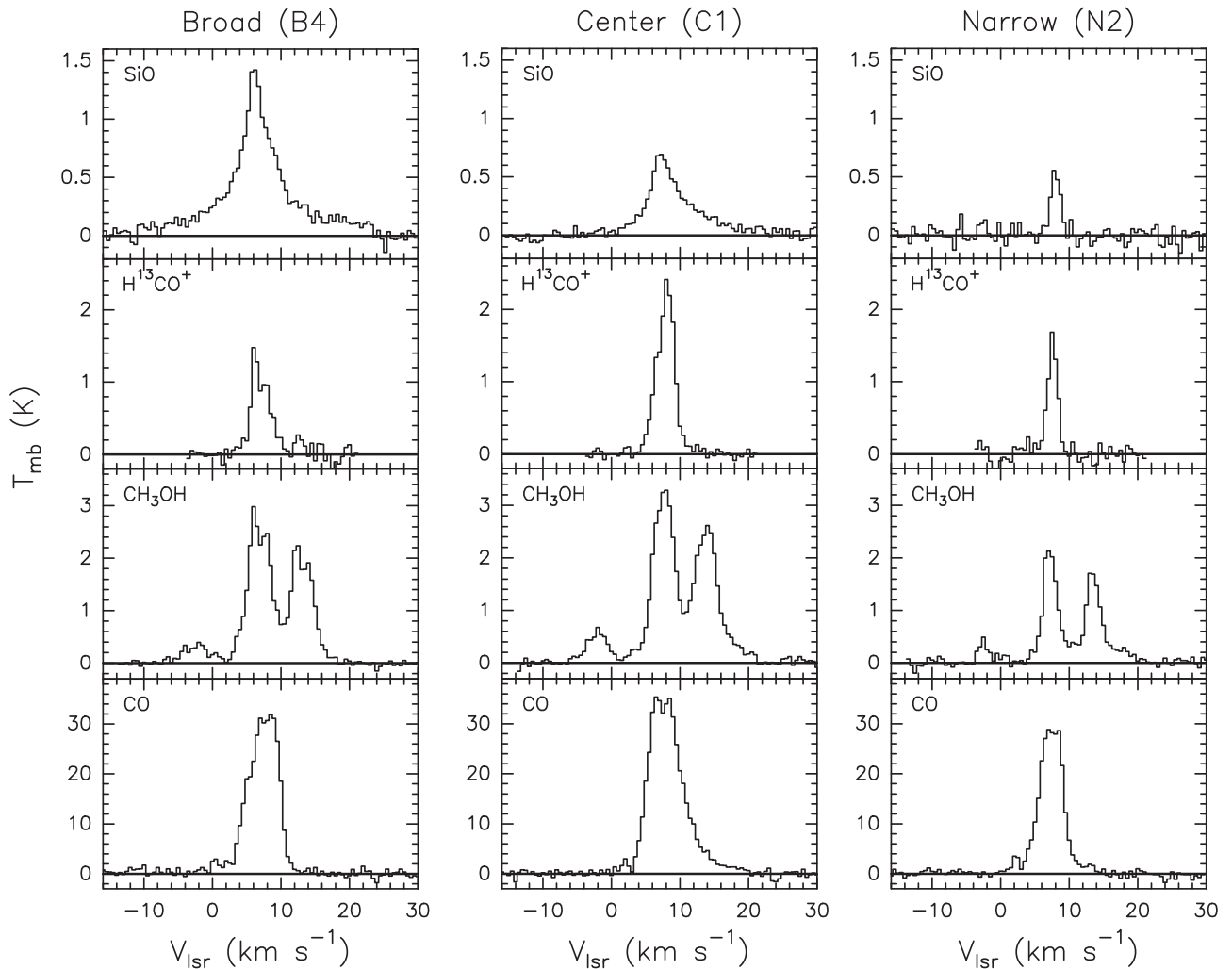


Figure 3. Sample spectra of CO, CH₃OH, H¹³CO⁺, and SiO, extracted from the offset positions of B4, C1, and N2 (see Table 3 and labels in Figure 2), illustrating, respectively, the three components that we distinguish: broad (left), central (middle), and narrow (right), as described in the main text. The average systemic velocity across NGC 2264-C is 7.5 km s⁻¹.

blue- and redshifted line wings, as indicated in column 3 of Table 3. The velocity ranges used in the integration were determined by comparing the CO line with the H¹³CO⁺ line and following the same approach described in López-Sepulcre et al. (2009): we defined the low-velocity limits where the line intensity of H¹³CO⁺ falls below 2σ , and the high-velocity limits where the line intensity of the two outflow tracers falls below 2σ . For SiO, we provide two estimates of the column density: one that includes only the blue- and redshifted line wings (N_{SiO} (blue) and N_{SiO} (red)), as in the case of CO, and one that includes the total column density of SiO integrated across the entire velocity range where the emission exceeds 2σ (N_{SiO} (tot)).

The resulting column densities, again adopting $T_{\text{ex}} = 10, 20,$ and 40 K, are listed in Table 5. We note that while the SiO emission is mostly optically thin across the whole velocity range, that of CO is moderately optically thick even in the high-velocity wings. The velocity-averaged optical depth in the CO wings ranges between 0.04 and 3.9 depending on the offset position and the excitation temperature adopted, with typical values of 0.12 ($T_{\text{ex}} = 40$ K) and 0.9 ($T_{\text{ex}} = 10$ K). These optical depths are taken into account in the derivation of column densities, as detailed in Section 4.1.

4.3. Molecular Abundances

Finally, we estimated the SiO abundance at each selected position. For the narrow component, we adopted a fixed HCO⁺ abundance across the region of 5×10^{-9} with respect to H₂. While this may introduce some uncertainty in the abundance derivation, several studies show that the abundance of HCO⁺ does not vary significantly from this value between outflows and dense cores (see Sánchez-Monge et al. 2013 and references therein). Since we observed the ¹³C isotopologue of HCO⁺, we adopted $^{12}\text{C}/^{13}\text{C} = 60$, as in Watanabe et al. (2015). With these assumptions, the derived SiO abundances are on the order of a few times 10^{-11} for the narrow component. The values are reported in column 6 of Table 4.

Estimates of the CH₃OH abundance are also provided in column 7 of Table 4 for the narrow component. The methanol abundance associated with the high-velocity gas cannot be reliably determined due to line blending with two other transitions of the same species, as mentioned earlier.

Since H¹³CO⁺ displays no detectable extended line wings, we cannot use this tracer to determine the SiO abundance of the high-velocity gas for the broad and central components. Instead, we used the column densities obtained for the extended

Table 3
Velocity Ranges and Line Fluxes Measured in Each Selected Position

Label ^a	$(\Delta x, \Delta y)^b$ (", ")	ΔV (km s ⁻¹)	$\int T_{\text{mb}} dV$ [H ¹³ CO ⁺] ^c (K km s ⁻¹)	$\int T_{\text{mb}} dV$ [SiO] (K km s ⁻¹)	$\int T_{\text{mb}} dV$ [CH ₃ OH] ^d (K km s ⁻¹)	$\int T_{\text{mb}} dV$ [CO] (K km s ⁻¹)
Narrow Component (N)						
N1 (ctr)	(9.0, 90.0)	[5.2, 9.2]	2.2 (0.7)	0.58 (0.19)	3.2 (0.9)	...
N2 (ctr)	(-96.0, 37.0)	[6.2, 8.8]	2.7 (0.8)	0.72 (0.22)	4.4 (1.3)	...
N3 (ctr)	(-105.0, 58.0)	[6.8, 9.8]	2.5 (0.7)	0.70 (0.22)	3.4 (1.0)	...
N4 (ctr)	(81.0, -29.0)	[4.8, 11.8]	3.4 (1.0)	1.1 (0.3)	3.8 (1.1)	...
N5 (ctr)	(-81.0, 71.0)	[6.5, 10.0]	3.0 (0.9)	0.97 (0.30)	4.6 (1.4)	...
Broad Component (B)						
CMM2 (blue)		[-1.2, 4.8]	...	1.1 (0.3)	...	34 (10)
CMM2 (red)		[8.2, 22.8]	...	2.6 (0.8)	...	60 (18)
CMM5 (ctr)	(-31.7, 23.8)	[5.2, 10.8]	7.8 (2.3)	4.6 (1.4)	15 (4)	...
CMM5 (blue)		[0.8, 5.2]	...	1.1 (0.3)	...	40 (12)
CMM5 (red)		[10.8, 20.8]	...	3.1 (0.9)	...	61 (18)
CMM9 (ctr)	(41.4, 23.9)	[4.8, 8.8]	4.3 (1.3)	3.1 (0.9)	8.6 (2.6)	...
CMM9 (blue)		[-9.2, 4.8]	...	3.2 (1.0)	...	22 (7)
CMM9 (red)		[8.8, 28.8]	...	3.2 (1.0)	...	34 (10)
CMM11 (ctr)	(-61.1, 47.6)	[5.8, 9.8]	6.0 (1.8)	2.8 (0.8)	8.5 (2.6)	...
CMM11 (blue)		[1.8, 5.8]	...	0.76 (0.23)	...	40 (12)
CMM11 (red)		[9.8, 25.8]	...	2.3 (0.7)	...	33 (10)
CMM12 (ctr)	(-37.0, 38.8)	[5.2, 11.2]	7.6 (2.3)	7.1 (2.1)	16 (5)	...
CMM12 (blue)		[-5.2, 5.2]	...	2.1 (0.6)	...	43 (13)
CMM12 (red)		[11.2, 25.8]	...	3.9 (1.2)	...	43 (13)
B1 (ctr)	(37.0, 2.0)	[4.8, 7.8]	4.2 (1.3)	1.8 (0.5)	7.1 (2.1)	...
B1 (blue)		[-1.2, 4.8]	...	1.2 (0.4)	...	23 (7)
B1 (red)		[7.8, 22.8]	...	3.6 (1.1)	...	73 (22)
B2 (ctr)	(-11.0, -64.0)	[5.8, 10.2]	2.8 (0.8)	2.5 (0.7)	11 (3)	...
B2 (blue)		[-1.2, 5.8]	...	0.63 (0.20)	...	18 (5)
B2 (red)		[10.2, 24.8]	...	5.8 (1.7)	...	47 (14)
B3 (ctr)	(1.0, 43.0)	[5.2, 9.8]	4.5 (1.4)	3.9 (1.2)	9.4 (2.8)	...
B3 (blue)		[0.8, 5.2]	...	1.0 (0.3)	...	17 (5)
B3 (red)		[9.8, 20.8]	...	3.6 (1.1)	...	43 (13)
B4 (ctr)	(37.0, -31.0)	[5.2, 9.2]	3.6 (1.1)	3.8 (1.1)	9.0 (2.7)	...
B4 (blue)		[-6.5, 5.2]	...	3.9 (1.2)	...	35 (11)
B4 (red)		[9.2, 23.5]	...	3.1 (0.9)	...	33 (10)
Central Component (C)						
CMM3 (blue)		[-2.2, 4.8]	...	0.95 (0.29)	...	16 (5)
CMM3 (red)		[10.2, 22.8]	...	2.0 (0.6)	...	31 (9)
CMM13 (ctr)	(-12.9, 4.7)	[4.8, 10.8]	7.8 (2.3)	3.0 (0.9)	14 (4)	...
CMM13 (blue)		[-1.2, 4.8]	...	0.50 (0.16)	...	16 (5)
CMM13 (red)		[10.8, 17.8]	...	1.1 (0.3)	...	32 (10)
C1 (ctr)	(-8.0, -11.0)	[4.8, 10.8]	7.1 (2.1)	2.7 (0.8)	13 (4)	...
C1 (blue)		[1.8, 4.8]	...	0.43 (0.14)	...	13 (4)
C1 (red)		[10.8, 18.8]	...	1.2 (0.4)	...	36 (11)
C2 (ctr)	(-3.0, 18.5)	[5.2, 9.8]	6.3 (1.9)	2.9 (0.9)	12 (4)	...
C2 (blue)		[-1.2, 5.2]	...	0.84 (0.26)	...	27 (8)
C2 (red)		[9.8, 17.8]	...	1.4 (0.4)	...	43 (13)
C3 (ctr)	(-23.0, 2.5)	[5.2, 10.8]	7.4 (2.2)	2.7 (0.8)	13 (4)	...
C3 (blue)		[-0.2, 5.2]	...	0.52 (0.17)	...	23 (7)
C3 (red)		[10.8, 18.8]	...	1.4 (0.4)	...	52 (16)

Notes.

^a The label in brackets indicates whether the velocity range used corresponds to the central velocities (ctr), the blueshifted wing (blue), or the redshifted wing (red).

^b Offset coordinates with respect to the reference position: R.A.(J2000) = 06^h41^m12^s.3, decl.(J2000) = 09°29'11"90.

^c High-velocity emission is not detected for H¹³CO⁺($J = 1 - 0$).

^d No line flux measured at the line wings due to blending with two other CH₃OH lines.

wings of the CO lines by adopting a CO abundance of 10^{-4} with respect to H₂. The SiO abundances derived in this manner are listed in columns 8 and 9 of Table 5 for the blue- and

redshifted line wings, respectively. They are on the order of 10^{-9} – 10^{-8} , with the central component having smaller abundances than the broad component by a factor of 2–3.

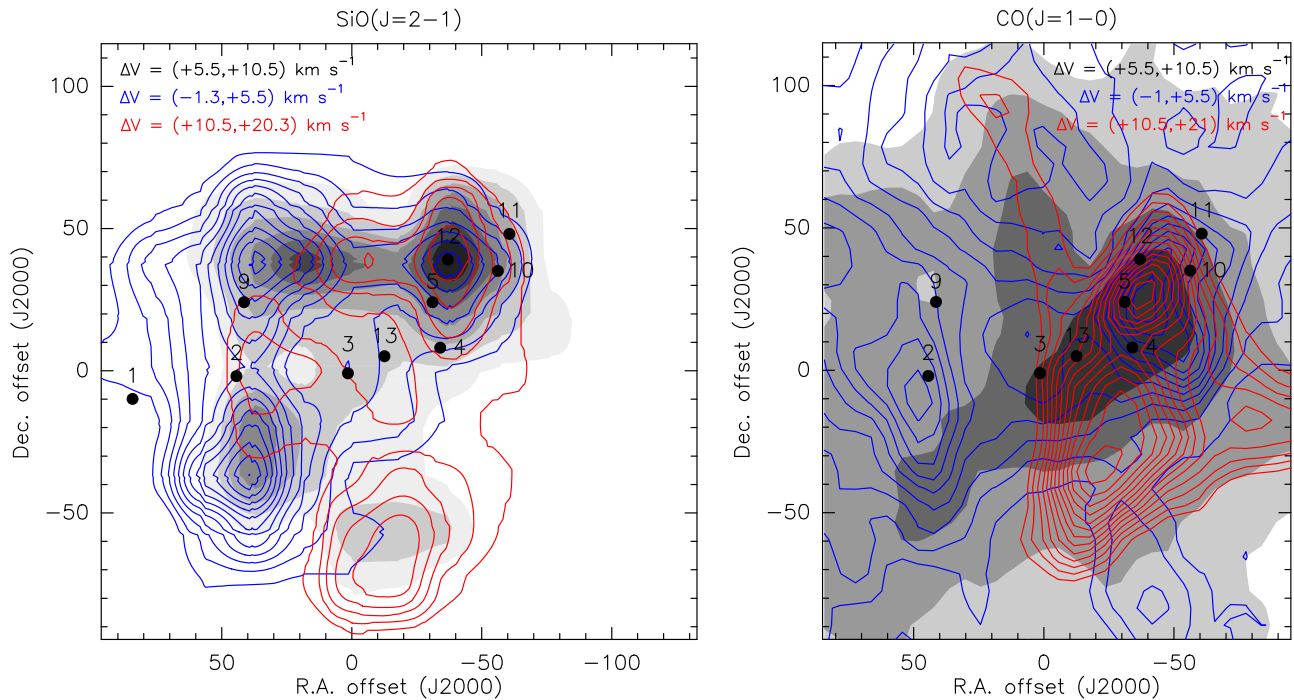


Figure 4. SiO and CO outflow maps. Blue and red contours correspond to the blue- and redshifted high-velocity wings, as indicated in the key and in Table 2. The gray scale corresponds to the central velocities, as indicated in the key, with contours starting at 30% (SiO) and 50% (CO) of the peak intensity and increasing by steps of 10%. The peak intensity is 6.7 and 172 K km s⁻¹ for the SiO and CO grayscale, respectively. Contours for the SiO outflow maps start at 5 σ and increase by steps of 3 σ , while for the CO maps they start at 25 σ and increase by steps of 5 σ (see Table 2). Black circles mark the positions of the cores identified by Peretto et al. (2006, 2007).

For consistency, we also derived a lower limit to the SiO abundance using a 2 σ upper limit on the H¹³CO⁺ column density at high velocities. The resulting values are on the order of 10⁻⁹ or smaller, and therefore are consistent with the abundances obtained using the CO column densities.

Table 6 summarizes, for each component, the mean column densities and abundances of the sample of selected positions in Figure 2, along with their standard deviations. For the broad and central components, two SiO column density estimates are provided, as explained in Section 4.2: one that considers only the high-velocity gas, B and C, and one that considers the total amount of gas including ambient and high velocities, B (tot) and C (tot). For the undetected line wings of H¹³CO⁺, a 2 σ upper limit is provided.

Several points can be extracted from this table. First, while the narrow component shows little dispersion in the SiO and H¹³CO⁺ column densities, resulting in a low dispersion of the mean SiO abundance, the broad component has a more scattered range of SiO and CO column densities, which results in a large dispersion of the mean SiO abundance. The central component has a low scatter in the SiO column density values, but a high one for CO, which yields a large dispersion for the mean SiO abundance. Second, the abundances of SiO and CH₃OH vary by less than a factor of 2 from $T_{\text{ex}} = 10$ K to $T_{\text{ex}} = 40$ K. The column densities differ by a factor lower than 2 for all the molecules, except for CH₃OH, for which the difference rises up to a factor of 4. Finally and most importantly, the abundance of SiO in the narrow component is more than two orders of magnitude lower than that in the central and broad components. In addition, the central component appears less abundant in SiO than the broad component by an average factor of 2.

5. DISCUSSION

In the present section, we discuss the narrow, broad, and central components on the basis of our results and those reported in the literature.

5.1. Central SiO Depletion

Figure 5 shows the total column densities of SiO, H¹³CO⁺, and CH₃OH, which are derived assuming $T_{\text{ex}} = 10$ K for each selected position in Table 3 and plotted as a function of radial distance from CMM3, i.e., roughly the center of the clump. The plots for $T_{\text{ex}} = 20$ and 40 K are qualitatively very similar. The SiO plot clearly highlights the three distinct components that we identified in Section 3.2. If we concentrate on the shortest radial distances, then it is evident that the column density is almost a factor of 3 lower within a radius of 25'' (0.09 pc) from the center than at larger distances up to about 60'' (0.22 pc) where the strongest SiO emission can be seen in Figure 1.³ This decrease in the amount of gaseous SiO toward the center of the protocluster contrasts with the column density profile of H¹³CO⁺, which peaks at the center and gradually decreases with increasing radial distance.

Therefore, it appears that the central area of NGC 2264-C has a relative depletion of SiO despite it showing signs of protostellar outflow activity, as acknowledged from (i) the high-velocity wings present in the SiO line profiles and (ii) the CO outflow maps reported by Maury et al. (2009). Depletion of gaseous SiO may occur through freeze-out back onto dust grains, which has a reported timescale of $\sim 10^4$ years (Bergin

³ Note that there is a slight enhancement at the position of CMM3, but this is likely due to the presence of a compact outflow driven by this source (Saruwatari et al. 2011).

Table 4
Narrow Component: Column Densities and Abundances in Each Selected Position

Label	T_{ex} (K)	N_{SiO} (10^{12} cm^{-2})	$N_{\text{CH}_3\text{OH}}$ (10^{14} cm^{-2})	$N_{\text{H}_3\text{CO}^+}$ (10^{12} cm^{-2})	χ_{SiO} (10^{-11})	$\chi_{\text{CH}_3\text{OH}}$ (10^{-9})
CMM1	10	2.1 ± 0.8	4.0 ± 1.2	3.2 ± 1.2	5.3 ± 2.8	10 ± 5
	20	2.7 ± 1.0	7.2 ± 2.2	4.5 ± 1.6	5.0 ± 2.6	13 ± 6
	40	4.4 ± 1.7	17 ± 5	7.6 ± 2.8	4.8 ± 2.5	19 ± 9
N1	10	1.3 ± 0.6	2.8 ± 0.9	2.7 ± 0.9	4.0 ± 2.4	8.8 ± 4.1
	20	1.7 ± 0.8	5.0 ± 1.6	3.7 ± 1.3	3.8 ± 2.2	11 ± 5
	40	2.7 ± 1.3	12 ± 4	6.3 ± 2.3	3.6 ± 2.2	16 ± 8
N2	10	1.6 ± 0.6	4.1 ± 1.2	3.4 ± 1.1	3.9 ± 1.8	10 ± 4
	20	2.1 ± 0.7	7.1 ± 2.1	4.7 ± 1.5	3.7 ± 1.8	13 ± 5
	40	3.4 ± 1.2	17 ± 5	7.8 ± 2.5	3.6 ± 1.7	18 ± 8
N3	10	1.6 ± 0.6	3.1 ± 0.9	3.1 ± 0.9	4.3 ± 2.1	8.4 ± 3.6
	20	2.0 ± 0.8	5.5 ± 1.6	4.2 ± 1.3	4.1 ± 2.0	11 ± 5
	40	3.3 ± 1.3	13 ± 4	7.0 ± 2.2	3.9 ± 2.0	15 ± 7
N4	10	2.3 ± 1.1	3.4 ± 1.0	4.1 ± 1.3	4.8 ± 2.7	7.0 ± 3.1
	20	3.0 ± 1.4	6.1 ± 1.8	5.7 ± 1.9	4.5 ± 2.6	9.0 ± 4.0
	40	5.0 ± 2.3	15 ± 4	9.6 ± 3.2	4.3 ± 2.5	13 ± 6
N5	10	2.2 ± 0.8	4.4 ± 1.2	3.9 ± 1.2	4.6 ± 2.2	9.3 ± 3.8
	20	2.8 ± 1.0	7.5 ± 2.2	5.3 ± 1.7	4.4 ± 2.1	12 ± 5
	40	4.5 ± 1.6	18 ± 5	8.8 ± 2.8	4.3 ± 2.1	17 ± 7

et al. 1998). It may also be destroyed via a neutral-neutral reaction with OH, yielding SiO₂, which has no activation barrier. This reaction is slow, with a constant rate of $2 \times 10^{-12} \text{ cm}^3 \text{ s}^{-1}$ (KIDA database⁴, Wakelam et al. 2012), but it is expected to be effective in outflow regions due to the enhanced abundances of OH in shocks (see, e.g., Ceccarelli et al. 1998; Goicoechea et al. 2006, where OH abundances of $\sim 10^{-6}$ are measured). The reported timescale of this reaction is also on the order of 10^4 years (Pineau des Forêts et al. 1997). However, both in the case of SiO depletion onto dust grains and of SiO gas-phase destruction, the quoted timescales assume a gas volume density of 10^5 cm^{-3} . The density around the center of NGC 2264-C is calculated to be higher than 10^6 cm^{-3} and as high as 10^8 cm^{-3} (see Figure 9 in Peretto et al. 2006). In these high-density conditions, the depletion of gaseous SiO is expected to be much faster, as fast as a few hundred years. Thus, we may be seeing the result of the partial destruction/depletion of SiO in this central region.

An analogous behavior has been reported in, e.g., the low-mass protostar NGC 1333 IRAS 2A, where SiO emission becomes weaker very close to the driving source due to the enhanced density (Jørgensen et al. 2004). However, the radial distances involved in that case are on the order of 10^3 au and they concern an individual protostar, while in our case we measure a radial distance two orders of magnitude larger: it is a protocluster rather than a protostar effect.

Methanol (CH₃OH), on the other hand, does not show evidence of central depletion in Figure 5. However, it should be kept in mind that, for this molecule, we have only integrated the emission at the central line velocities to obtain its column density. The values in this plot should thus be taken as lower limits and are subject to larger errors than the other two molecules. The column densities derived for the narrow (N) component are most likely closer to the actual values than those of the central (C) and broad (B) components, since the line widths are narrower and thus less line flux has been missed in the calculation. Nevertheless, this plot, as well as the CH₃OH map in Figure 1, indicates that this molecule's emission is

relatively stronger at the center than SiO. Therefore, CH₃OH does not suffer the same kind of partial depletion as SiO in the inner region of the protocluster. This may be due to the higher degree of volatility of CH₃OH and the high temperatures close to the presumed hot core within CMM3 (Watanabe et al. 2015), which favor the direct vaporization of methanol from grain mantles through heating. Indeed, methanol will be significantly sublimated from the mantles at temperatures above 85 K (Brown & Bolina 2007). CH₃OH may also be released into the gas as a result of protostellar shocks, but depletion back onto dust grains would not occur as rapidly as for SiO, especially if temperatures are not very low (e.g., Yanagida et al. 2014).

5.2. Narrow SiO Emission: A Tracer of a Previous Star Formation Episode?

The top panel in Figure 5 clearly shows how, beyond a radial offset of $80''$ (i.e., ~ 0.3 pc) from the center, the total SiO column density decreases drastically by one order of magnitude. The change is even more pronounced in terms of abundance, where the difference is of more than two orders of magnitude with respect to the broad component (see Table 6). As discussed above, the SiO lines are also much narrower here, with average an FWHM of 2 km s^{-1} and no detectable high-velocity wings. This kind of SiO line profile has been reported in several other star-forming regions (e.g., Lefloch et al. 1998; Hatchell et al. 2001; Jiménez-Serra et al. 2010; Duarte-Cabral et al. 2014). As in the present work, all of these studies report an SiO abundance with respect to H₂ around 10^{-11} – 10^{-10} for such a low-velocity component, i.e., much lower than the abundances typically associated with fast outflow shocks (10^{-9} – 10^{-7} ; e.g., Bachiller & Pérez-Gutiérrez 1997; Sánchez-Monge et al. 2013, this work). The abundances associated with this narrow SiO emission are, however, higher than those found in dark clouds ($\lesssim 10^{-12}$; Ziurys et al. 1989; Requena-Torres et al. 2002). Therefore, something must be causing this slight enhancement of gaseous SiO.

A possible explanation for this low-velocity SiO component, first proposed by Lefloch et al. (1998) and Codella et al. (1999), is that this emission traces old protostellar outflow shocks, which have decelerated and become significantly depleted in

⁴ <http://kida.obs.u-bordeaux1.fr/>

Table 5
Broad and Central Components: Column Densities and Abundances in Each Selected Position

Label	T_{ex} (K)	$N_{\text{SiO}}(\text{tot})^{\text{a}}$ (10^{12} cm^{-2})	$N_{\text{SiO}}(\text{blue})$ (10^{12} cm^{-2})	$N_{\text{SiO}}(\text{red})$ (10^{12} cm^{-2})	$N_{\text{CO}}(\text{blue})^{\text{b}}$ (10^{16} cm^{-2})	$N_{\text{CO}}(\text{red})$ (10^{16} cm^{-2})	$\chi_{\text{SiO}}(\text{blue})$ (10^{-9})	$\chi_{\text{SiO}}(\text{red})$ (10^{-9})
Broad Component (B)								
CMM5	20	16 ± 3	3.3 ± 1.2	7.6 ± 2.7	5.1 ± 1.4	8.7 ± 2.5	6.4 ± 2.9	8.7 ± 4.0
	40	27 ± 6	5.4 ± 1.9	12 ± 4	7.6 ± 2.2	13 ± 4	7.1 ± 3.3	9.3 ± 4.3
	10	20 ± 4	2.4 ± 0.8	7.0 ± 2.2	—	16 ± 2	—	4.4 ± 1.6
CMM9	20	26 ± 5	3.1 ± 1.1	9.0 ± 2.9	7.1 ± 1.8	9.6 ± 2.6	4.4 ± 1.9	9.4 ± 4.0
	40	42 ± 8	5.1 ± 1.7	15 ± 5	9.4 ± 2.7	14 ± 4	5.4 ± 2.4	10 ± 5
	10	21 ± 4	7.1 ± 2.3	7.0 ± 2.5	2.3 ± 0.8	3.7 ± 1.0	31 ± 13	19 ± 9
CMM11	20	28 ± 5	9.3 ± 3.1	9.2 ± 3.3	2.9 ± 0.9	4.6 ± 1.4	32 ± 14	20 ± 9
	40	45 ± 9	15 ± 5	15 ± 5	4.7 ± 1.4	7.3 ± 2.2	32 ± 14	21 ± 10
	10	13 ± 3	1.7 ± 0.5	5.2 ± 1.8	—	3.6 ± 1.0	—	14 ± 6
CMM12	20	17 ± 3	2.2 ± 0.7	6.7 ± 2.3	7.7 ± 1.8	4.4 ± 1.3	2.8 ± 1.1	15 ± 7
	40	28 ± 6	3.6 ± 1.2	11 ± 4	9.7 ± 2.7	7.0 ± 2.1	3.7 ± 1.6	16 ± 7
	10	31 ± 6	4.8 ± 1.7	8.7 ± 2.9	6.2 ± 1.5	5.3 ± 1.4	7.7 ± 3.3	17 ± 7
B1	20	39 ± 8	6.2 ± 2.2	11 ± 4	6.2 ± 1.8	6.0 ± 1.7	10 ± 5	19 ± 8
	40	62 ± 12	10 ± 4	18 ± 6	9.5 ± 2.8	9.4 ± 2.8	11 ± 5	20 ± 9
	10	15 ± 3	2.6 ± 1.1	8.1 ± 3.0	3.2 ± 0.8	12 ± 3	8.2 ± 3.9	6.5 ± 2.8
B2	20	19 ± 4	3.4 ± 1.4	11 ± 4	3.3 ± 0.9	11 ± 3	10 ± 5	9.6 ± 4.5
	40	31 ± 7	5.6 ± 2.3	17 ± 6	5.1 ± 1.5	16 ± 5	11 ± 6	10 ± 5
	10	20 ± 5	1.4 ± 0.7	13 ± 4	2.1 ± 0.6	5.9 ± 1.5	6.7 ± 4.0	22 ± 9
B3	20	26 ± 6	1.8 ± 1.0	17 ± 5	2.4 ± 0.7	6.5 ± 1.9	7.5 ± 4.6	26 ± 11
	40	42 ± 10	2.9 ± 1.6	27 ± 9	3.8 ± 1.1	10 ± 3	7.7 ± 4.7	27 ± 12
	10	20 ± 4	2.3 ± 0.8	8.1 ± 2.7	2.3 ± 0.6	6.0 ± 1.5	9.9 ± 4.3	13 ± 5
B4	20	25 ± 5	2.9 ± 1.1	11 ± 3	2.4 ± 0.7	6.2 ± 1.8	12 ± 6	17 ± 7
	40	41 ± 8	4.8 ± 1.8	17 ± 6	3.7 ± 1.1	9.5 ± 2.7	13 ± 6	18 ± 8
	10	25 ± 5	8.8 ± 3.0	6.9 ± 2.6	4.3 ± 1.1	3.7 ± 1.0	20 ± 9	19 ± 9
	20	32 ± 6	11 ± 4	8.9 ± 3.4	4.8 ± 1.4	4.4 ± 1.3	23 ± 11	20 ± 10
	40	51 ± 10	18 ± 6	15 ± 6	7.6 ± 2.3	7.0 ± 2.1	24 ± 11	21 ± 10
	Central Component (C)							
CMM13	20	18 ± 4	2.7 ± 1.1	5.7 ± 2.2	2.2 ± 0.7	4.2 ± 1.2	12 ± 6	14 ± 7
	40	29 ± 6	4.5 ± 1.9	9.4 ± 3.6	3.5 ± 1.1	6.6 ± 2.0	13 ± 7	14 ± 7
	10	10 ± 2	1.1 ± 0.5	2.4 ± 0.9	1.9 ± 0.5	4.9 ± 1.1	5.8 ± 3.2	4.9 ± 2.1
C1	20	13 ± 3	1.4 ± 0.7	3.2 ± 1.1	2.2 ± 0.6	4.6 ± 1.3	6.6 ± 3.7	6.8 ± 3.1
	40	22 ± 5	2.4 ± 1.1	5.2 ± 1.9	3.4 ± 1.0	7.0 ± 2.1	6.9 ± 3.8	7.3 ± 3.4
	10	10 ± 2	0.9 ± 0.4	2.8 ± 1.1	2.0 ± 0.5	5.6 ± 1.3	4.8 ± 2.2	4.9 ± 2.2
C2	20	13 ± 3	1.2 ± 0.5	3.6 ± 1.4	1.9 ± 0.5	5.2 ± 1.5	6.5 ± 3.1	6.8 ± 3.2
	40	21 ± 5	2.0 ± 0.8	5.9 ± 2.3	2.9 ± 0.9	8.0 ± 2.4	6.9 ± 3.4	7.3 ± 3.6
	10	12 ± 3	1.9 ± 0.9	3.2 ± 1.3	3.9 ± 0.9	7.9 ± 1.6	4.8 ± 2.6	4.1 ± 1.8
C3	20	15 ± 3	2.4 ± 1.2	4.2 ± 1.7	3.9 ± 1.1	6.4 ± 1.8	6.3 ± 3.5	6.5 ± 3.1
	40	25 ± 5	3.9 ± 1.9	6.8 ± 2.7	5.9 ± 1.7	9.5 ± 2.8	6.7 ± 3.8	7.1 ± 3.5
	10	10 ± 2	1.2 ± 0.6	3.1 ± 1.2	3.2 ± 0.8	19 ± 2	3.6 ± 2.1	1.6 ± 0.7
	20	14 ± 3	1.5 ± 0.8	4.0 ± 1.6	3.3 ± 0.9	8.3 ± 2.2	4.6 ± 2.9	4.9 ± 2.3
	40	22 ± 5	2.5 ± 1.4	6.6 ± 2.7	5.0 ± 1.5	12 ± 3	4.9 ± 3.1	5.5 ± 2.7

Notes.

^a Total column density of SiO, obtained by integrating the emission over the entire velocity range.

^b —: the observed line flux is under-reproduced at the indicated value of T_{ex} .

SiO over time. Codella et al. estimated the deceleration timescale to be on the order of 10^4 years, the same timescale in which SiO would have been largely depleted back onto dust grains and/or destroyed in the gas phase via reactions with OH. This scenario is consistent with both the narrow SiO line profile and the relatively low SiO abundance.

To evaluate whether this could be the case in NGC 2264-C, we consider both the spatial distribution of the narrow SiO emission in Figures 1 and 2, and the dynamical age of the molecular outflows identified by Maury et al. (2009). The narrow SiO component is distributed mostly near the northern and eastern edges of the protocluster, which is sufficiently close to the tips of several CO outflows identified by Maury et al.

These CO outflows have reported dynamical ages of $\sim 10^4$ years. Therefore, it is possible that the narrow SiO emission is tracing older shocks from such molecular outflows which have decelerated to ambient velocities. At the radial distance where the low-velocity component is located, the average gas density is on the order of 10^5 cm^{-3} (Peretto et al. 2006), and thus is also consistent with a depletion timescale of about 10^4 years (Bergin et al. 1998). However, as can be seen in Figure 5, the radial change in column density is rather sudden from the broad to the narrow component positions, and the abundance decrease is even steeper. One would expect a more gradual gradient if the low-velocity SiO

Table 6
Average Molecular Column Densities and Abundances for Each Component^a

Comp. ^b	\bar{N}_{SiO} (10^{12} cm^{-2})	$\bar{N}_{\text{CH}_3\text{OH}}$ (10^{14} cm^{-2})	$\bar{N}_{\text{H}_2\text{CO}^+}$ (10^{12} cm^{-2})	\bar{N}_{CO} (10^{16} cm^{-2})	$\bar{\chi}_{\text{SiO}}$ ^c (10^{-11})	$\bar{\chi}_{\text{CH}_3\text{OH}}$ ^c (10^{-9})
$T_{\text{ex}} = 10 \text{ K}$						
B	5.8 ± 3.1	...	<6.8	5.8 ± 3.6	1300 ± 1200	...
B (tot)	20 ± 5	...	6.6 ± 2.4
C	2.3 ± 1.0	...	<4.3	5.4 ± 5.0	580 ± 510	...
C (tot)	11 ± 1	...	9.8 ± 0.8
$T_{\text{ex}} = 20 \text{ K}$						
B	7.5 ± 4.0	...	<11.7	5.7 ± 2.4	1400 ± 1400	...
B (tot)	25 ± 7	...	8.7 ± 3.0
C	3.0 ± 1.4	...	<6.1	4.2 ± 1.9	750 ± 620	...
C (tot)	15 ± 2	...	13 ± 1
$T_{\text{ex}} = 40 \text{ K}$						
B	12 ± 6	...	<17	8.6 ± 3.3	1500 ± 1400	...
B (tot)	41 ± 11	...	14 ± 5
C	4.9 ± 2.2	...	<10	6.4 ± 2.8	800 ± 650	...
C (tot)	24 ± 3	...	21 ± 2

Notes.

^a The values given are the mean of all the selected positions for each component and its standard deviation. For CH₃OH and H¹³CO⁺, only the narrow component is considered, while for CO only the broad and central components are taken into account (see text).

^b Column densities for B (tot) and C (tot) refer to those integrated across the whole velocity range of the emission line. Column densities for B and C refer to those of the blue- and redshifted high-velocity emission (see text).

^c Abundance with respect to H₂.

emission were due to the ageing of the molecular outflow as it travels further away from its driving source.

An alternative explanation for such a drastic spatial change in the SiO abundance is the following. NGC 2264-C is known to have experienced more than one episode of star formation. It might be possible that the narrow SiO emission seen in this region has its origin in the star formation episode that preceded the one that is currently taking place. If this is so, then the astrochemical remnants of that previous episode would have been replaced by those of the current protostellar activity everywhere but in the most external areas of the protocluster where contamination from current outflows is less important. It is not obvious to unambiguously identify such a stellar population, as it may be deeply embedded in the gas, and thus be undetectable/unresolvable at the angular resolution of our observations. Furthermore, the known young stars detected in infrared studies (Lada et al. 1993) may be the result of an even earlier star formation episode (their ages are 10⁵–10⁶ years), and a K-band source is also known to reside close to CMM3 (Schreyer et al. 1997, 2003). These evolved sources are thus unlikely to be responsible for the narrow SiO component detected. Perhaps the previous star formation episode is related to the B2-type zero-age main-sequence star, IRS1, to the north-west of NGC 2264-C (Allen 1972; Thompson et al. 1998). This high-mass star opens up a cavity that is 0.1 pc in diameter, and it is surrounded by a shell of molecular gas that contains the cores CMM5, CMM10, CMM11, and CMM12, which are believed to be the result of star formation triggered by IRS1. While this is merely speculation, IRS1 might be part of the stellar population that formed before the younger cores at the center and east of the protocluster. Indeed, a large fraction of the narrow SiO emission is located to the north and west of IRS1.

5.3. Other Possible Origins of the Narrow SiO Emission

We have discussed above how the narrow SiO emission we detect may be tracing a previous episode of star formation in NGC 2264-C. In this section, we explore alternative explanations. For instance, Jiménez-Serra et al. (2010) proposed that such narrow SiO lines could be produced by low-velocity shocks due to large-scale flow collisions during global cloud collapse. The authors argued that shock velocities of $\sim 12 \text{ km s}^{-1}$ could account for the SiO gas abundances of about 10^{-11} observed in the infrared-dark cloud (IRDC) G35.39–00.33. This scenario is also favored by Duarte-Cabral et al. (2014), who performed interferometric observations of SiO($J = 2 - 1$) in the high-mass star-forming complex Cygnus X. They proposed an evolutionary picture in which the earliest stages of protocluster formation are characterized by extended, low-velocity SiO emission that traces shocks from the large-scale collapse of material onto them. At later stages, when star formation becomes more active and single massive protostars are formed, the SiO luminosity is largely dominated by powerful outflows, and the weaker narrow component shows the last remnants of the initial collapse. If this is the case for NGC 2264-C, then we could be witnessing the later evolutionary stages mentioned by Duarte-Cabral et al., where the multiple outflows present dominate the SiO emission and the last hints of large-scale collapse can only be seen at the outskirts of the region in the form of narrow and weak SiO lines.

Peretto et al. (2006) found that NGC 2264-C is indeed undergoing global infall along the axis connecting CMM2, CMM3, and CMM4. However, they measure an infall velocity of 1.3 km s^{-1} , which is rather small to produce the observed amounts of narrow SiO emission according to Jiménez-Serra et al. (2010). Furthermore, most of the narrow SiO emission is

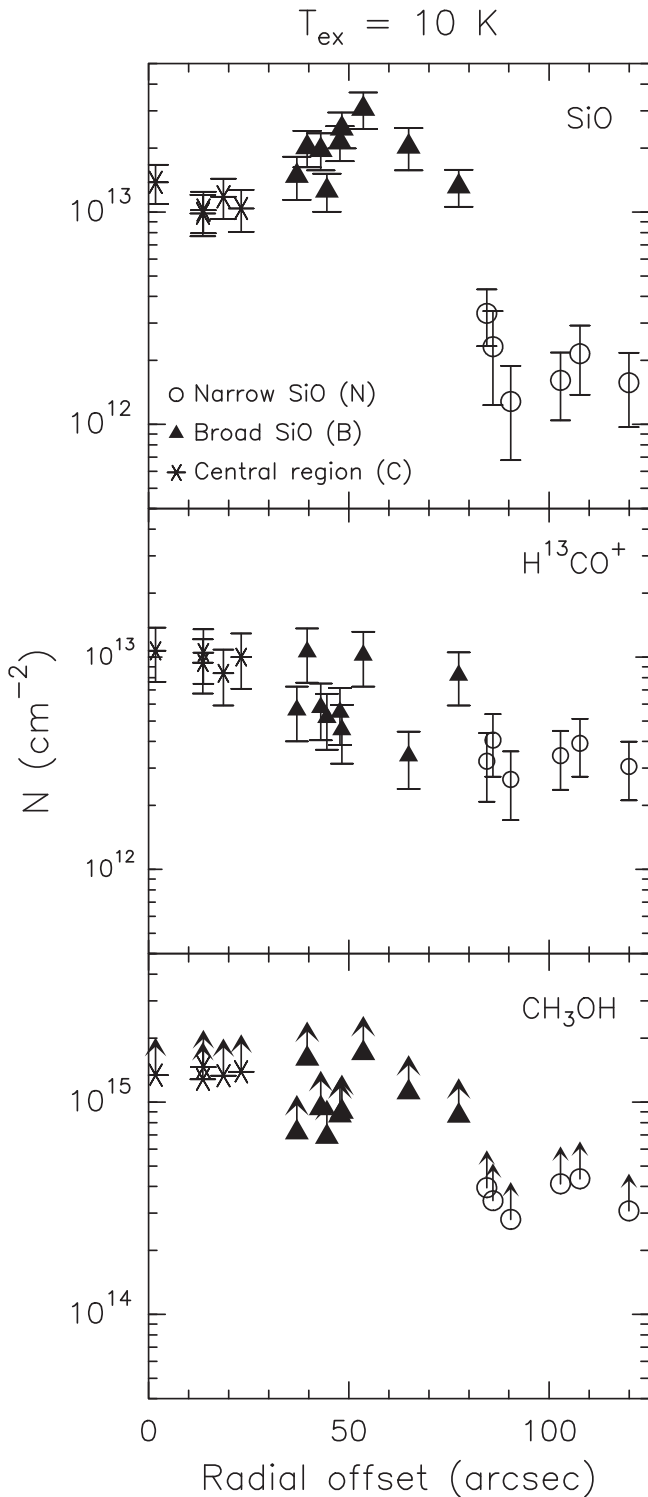


Figure 5. Total column density of SiO (top), H^{13}CO^+ (middle), and CH_3OH (bottom), as a function of radial offset with respect to the reference position, for an excitation temperature of 10 K. Note that for CH_3OH , the values are lower limits, particularly for the broad and central components, since only the central velocities were considered in the column density derivation. The reference ($0''$, $0''$) position corresponds to R.A.(J2000) = $06^{\text{h}}41^{\text{m}}12^{\text{s}}.3$, decl.(J2000) = $09^{\circ}29'11''.90$.

concentrated toward the north of the clump, a direction that is almost perpendicular to that reported for the global infall by Peretto et al. (2006).

The northern narrow SiO emission might instead be caused by low-velocity shocks due to the interaction of NGC 2264-C with NGC 2264-D, which lies about 1 pc north (see Figure 1 in Peretto et al. 2006), an option that was considered to be likely in the IRDC G28.23–00.19 by Sanhueza et al. (2013). In NGC 2264-C, however, this may not be the most likely possibility, since the line-of-sight velocity difference between the two clumps is 2 km s^{-1} , and there is no clear evidence of cloud-cloud collision between NGC 2264-C and D in the dynamical analysis reported by Peretto et al. (2006, 2007).

In summary, the velocities involved in and around NGC 2264-C seem to be insufficient to produce the observed amounts of SiO in low-velocity shocks due only to global collapse or cloud-cloud interaction. However, if there is some excess of silicon in the gas phase, especially if it is in the form of SiO, then lower-velocity shocks ($<10 \text{ km s}^{-1}$) can efficiently produce or maintain the observed amounts of gas-phase SiO (Nguyen-Lu’o’ng et al. 2013; Duarte-Cabral et al. 2014). As suggested in Section 5.2, SiO is likely enhanced in NGC 2264-C as a result of earlier high-velocity protostellar shocks. This implies that large-scale, low-velocity shocks in this region can only play a role if such SiO remnants from previous protostellar activity are present, which lends support to the scenario that we discussed in Section 5.2.

Alternatively, as first proposed by Jiménez-Serra et al. (2010), the low-velocity SiO component could be tracing an unresolved population of low-mass protostars. The beam dilution of the single-dish observations would cause the SiO high-velocity wings to be undetected. We can estimate whether a typical low-mass protostellar outflow might have the line wings of $\text{SiO}(J = 2 - 1)$ undetected at the distance of NGC 2264-C and at the angular resolution of our single-dish observations. The high-velocity SiO wings observed in SVS 13 by Lefloch et al. (1998), for instance, have intensities between 0.1 and 0.5 K in main-beam temperature units for a beam size of $24''$ (i.e., 5600 au at a distance of 235 pc; Hirota et al. 2008). Assuming that the low-mass outflow fills such a beam size (as inferred from the maps presented in Lefloch et al. 1998), and extrapolating it to the distance of NGC 2264-C, this corresponds to a size of $\sim 7''.5$. At an angular resolution of $20''$, the same SiO wings would have a beam-diluted intensity of 25–125 mK, which is indeed undetectable or just barely detectable at the sensitivity of our observations (see Table 1). Taking into account that the outflow driven by SVS 13 is rather powerful and that weaker—and more compact—outflows may be present, this is therefore a plausible alternative explanation for the narrow SiO emission.

Based on the different arguments exposed, we favor the scenario of old protostellar activity from a previous star formation episode or, alternatively, a population of unresolved low-mass protostars, to explain the narrow SiO emission detected in NGC 2264-C. Disentangling these possibilities would clearly benefit from high-angular resolution maps, as well as more SiO transitions to better constrain the properties of the SiO-emitting gas.

6. CONCLUSIONS

In order to study the role of SiO as a tracer of old protostellar shocks in large protoclusters, we have used the Nobeyama 45 m telescope to map the high-mass protocluster NGC 2264-C in $\text{SiO}(J = 2 - 1)$, as well as in $\text{H}^{13}\text{CO}^+(J = 1 - 0)$, $\text{CO}(J = 1 - 0)$, and $\text{CH}_3\text{OH}(2_0 - 1_0)$

A⁺), to further constrain the column densities and molecular abundances across the protocluster. Our main results can be summarized as follows.

1. A complex and tangled network of molecular outflows is present in this region that spans ~ 0.5 pc in size, as evidenced from the spatial distribution of the high-velocity line-wing emission of CO, SiO, and, to a lesser extent, CH₃OH.
2. We are able to identify three distinct SiO components in NGC 2264-C: (i) a broad component that is spatially offset with respect to the center of the protocluster, characterized by strong SiO emission and high-velocity wings indicative of protostellar outflow activity; (ii) a central component within the inner 0.2 pc of the molecular clump (i.e., around the massive molecular core CMM3) where the gas is densest, characterized by weaker SiO emission than in the broad component, but nevertheless exhibiting high-velocity wings suggestive of outflows; (iii) a narrow component, at the periphery of the region, where SiO lines are relatively weak and narrow.
3. While the column densities of H¹³CO⁺ and CH₃OH are enhanced at the center of NGC 2264-C, SiO appears to be relatively depleted in this area, with column densities that are a factor of 2 to 3 lower than in the more external, broad SiO component. At the high densities associated with the center of the protocluster, SiO destruction/depletion onto dust grains may occur on timescales of only 10^2 – 10^3 years. As a result, SiO appears to be relatively depleted despite the high outflow activity present. Beyond a radius of ~ 0.1 pc from the center, where the gas density is relatively lower, SiO depletion occurs in much longer timescales ($\sim 10^4$ years), which explains the stronger SiO emission of the broad component.
4. The SiO abundance with respect to H₂ associated with the peripheral narrow component in NGC 2264-C is $\sim 4 \times 10^{-11}$, i.e., more than two orders of magnitude lower than those associated with the broad and central components ($\sim 1.4 \times 10^{-8}$ and $\sim 4 \times 10^{-9}$, respectively). Such a low abundance of SiO is nevertheless higher than that associated with dark clouds ($\lesssim 10^{-12}$).
5. We propose that the narrow SiO component may be tracing the remnants of the star formation event that preceded the current one in NGC 2264-C. If this is the case, then the narrow SiO line emission would be providing astrochemical evidence that more than one star formation episode occurred in this region. Alternatively, an unresolved population of low-mass protostars could be responsible for the narrow SiO emission, where the non-detection of high-velocity wings would be due to beam dilution effects of the single-dish observations. Distinguishing between these two possibilities requires high-angular resolution mapping with interferometers.
6. Based on the low large-scale infall velocities associated with NGC 2264-C (~ 1.4 km s⁻¹), it is unlikely that low-velocity shocks from global collapse are responsible for the narrow SiO emission in this source. Similarly, low-velocity shocks due to cloud-cloud collapse can hardly justify the observed narrow SiO emission, since the projected velocity difference between NGC 2264-C and NGC 2264-D is of ~ 2 km s⁻¹. However, these possibilities should not be completely discarded before obtaining

larger maps and, ideally, multiple SiO transitions to better constrain the properties of the SiO-emitting gas.

Following the results of the present study, the role of SiO as a tracer of past star formation events should be further tested in this and other high-mass protocluster regions.

The authors are grateful to the NRO staff for their excellent support. The present study is supported by Grant-in-Aid from the Japanese Ministry of Education, Culture, Sports, Science, and Technologies (21224002, 25400223, and 25108005). We thank the anonymous referee for kindly devoting time to review the present manuscript.

Facility: NRO.

REFERENCES

- Allen, D. 1972, *ApJ*, **172**, 55
- Anderl, S., Guillet, V., Pineau des Forêts, G., & Flower, D. R. 2013, *A&A*, **556**, A69
- Bachiller, R., & Pérez-Gutiérrez, M. 1997, *ApJ*, **487**, 93
- Bergin, E. A., Melnick, G. J., & Neufeld, D. A. 1998, *ApJ*, **499**, 777
- Brown, W. A., & Bolina, A. S. 2007, *MNRAS*, **374**, 1006
- Ceccarelli, C., Caux, E., & White, G. J. 1998, *A&A*, **331**, 372
- Codella, C., Bachiller, R., & Reipurth, B. 1999, *A&A*, **343**, 585
- Codella, C., Cabrit, S., Gueth, F., et al. 2007, *A&A*, **462**, 53
- Duarte-Cabral, A., Bontemps, S., & Motte, F. 2014, *A&A*, **570**, A1
- Goicoechea, J. R., Cernicharo, J., & Lerate, M. R. 2006, *ApJL*, **641**, L49
- Gueth, F., Guilloteau, S., & Bachiller, R. 1998, *A&A*, **333**, 287
- Guillet, V., Jones, A. P., & Pineau Des Forêts, G. 2009, *A&A*, **497**, 145
- Gusdorf, A., Cabrit, S., Flower, D. R., et al. 2008, *A&A*, **482**, 809
- Hatchell, J., Fuller, G. A., & Millar, T. J. 2001, *A&A*, **372**, 281
- Hirota, T., Bushimata, T., Choi, Y. K., et al. 2008, *PASJ*, **60**, 37
- Jiménez-Serra, I., Caselli, P., Tan, J. C., et al. 2010, *MNRAS*, **406**, 187
- Jørgensen, J. K., Hogerheijde, M. R., Blake, G. A., et al. 2004, *A&A*, **415**, 1021
- Kamezaki, T., Imura, K., Omodaka, T., et al. 2014, *ApJS*, **211**, 18
- Krumholz, M. R., Bate, M. R., Arce, H. G., et al. 2014, in *Protostars and Planets VI*, ed. H. Beuther et al. (Tucson: Univ. Arizona Press), 243
- Krumholz, M. R., Klein, R. I., & McKee, C. F. 2007, *ApJ*, **656**, 959
- Krumholz, M. R., & McKee, C. F. 2008, *Natur*, **451**, 1082
- Lada, C. J., & Lada, E. A. 2003, *ARA&A*, **41**, 57
- Lada, C. J., Young, E. T., & Greene, T. P. 1993, *ApJ*, **408**, 471
- Lefloch, B., Castets, A., Cernicharo, J., & Loinard, L. 1998, *ApJ*, **504**, 109
- Li, Z.-Y., & Nakamura, F. 2006, *ApJ*, **640**, 187
- Longmore, S. N., Pillai, T., Keto, E., Zhang, Q., & Qiu, K. 2011, *ApJ*, **726**, 97
- López-Sepulcre, A., Codella, C., Cesaroni, R., Marcelino, N., & Walmsley, C. M. 2009, *A&A*, **499**, 811
- Matzner, C. D. 2007, *ApJ*, **659**, 1394
- Maury, A. J., André, Ph., & Li, Z.-Y. 2009, *A&A*, **499**, 175
- Nakamura, F., Kamada, Y., Kamazaki, T., et al. 2011, *ApJ*, **726**, 46
- Nakamura, F., & Li, Z.-Y. 2007, *ApJ*, **662**, 395
- Nguyen-Lu'o'ng, Q., Motte, F., Carlhoff, P., et al. 2013, *ApJ*, **775**, 88
- Peretto, N., André, Ph., & Belloche, A. 2006, *A&A*, **445**, 979
- Peretto, N., Hennebelle, P., & André, Ph. 2007, *A&A*, **464**, 983
- Pineau des Forêts, G., Flower, D. R., & Chieze, J.-P. 1997, in *IAU Symp. 182, Herbig-Haro Flows and the Birth of Stars*, ed. B. Reipurth, & C. Bertout (Dordrecht: Kluwer), 199
- Rebull, L. M., Makidon, R. B., Strom, S. E., et al. 2002, *AJ*, **123**, 1528
- Requena-Torres, M. A., Marcelino, N., Jiménez-Serra, I., et al. 2002, *ApJL*, **655**, L37
- Sánchez-Monge, Á, López-Sepulcre, A., Cesaroni, R., et al. 2013, *A&A*, **557**, 94
- Sanhueza, P., Jackson, J. M., Foster, J. B., et al. 2013, *ApJ*, **773**, 123
- Saruwatari, O., Sakai, N., Liu, S.-Y., et al. 2011, *ApJ*, **729**, 147
- Sawada, T., Ikeda, N., Sunada, K., et al. 2008, *PASJ*, **60**, 445
- Schreyer, K., Helmich, F. P., van ishoeck, E. F., & Henning, Th. 1997, *A&A*, **326**, 347
- Schreyer, K., Stecklum, B., Linz, H., & Henning, Th. 2003, *ApJ*, **599**, 335
- Stanke, T., & Williams, J. P. 2007, *AJ*, **133**, 1307
- Sung, H., Bessell, M. S., Chun, M.-Y., Karimov, R., & Ibrahimov, M. 2008, *AJ*, **135**, 441

- Sung, H., Bessell, M. S., & Lee, S-W. 1997, [AJ](#), 114, 2644
Tafalla, M., Bachiller, R., Lefloch, B., et al. 2015, [A&A](#), 573, L2
Thompson, R. I., Corbin, M. R., Young, E., & Schneider, G. 1998, [ApJL](#), 492, L177
Wakelam, V., Herbst, E., & Loison, J.-C. 2012, [ApJS](#), 199, 21
Watanabe, Y., Sakai, N., López-Sepulcre, A., et al. 2015, [ApJ](#), 809, 162
Yanagida, T., Sakai, T., Hirota, T., et al. 2014, [ApJL](#), 794, L10
Ziurys, L. M., Friberg, P., & Irvine, W. M. 1989, [ApJ](#), 343, 201